Optical probing of laser-induced indirectly driven shock waves in aluminum

M. Basko,* Th. Löwer, V. N. Kondrashov,† A. Kendl, R. Sigel,‡ and J. Meyer-ter-Vehn
Max-Planck-Institut für Quantenoptik, D-85748 Garching, Germany
(Received 25 March 1997)

Optical signals from shock waves emerging at a free surface of metals are expected to yield information about the equation of state and the transport and relaxation properties of hot dense plasmas. We present the results of optical measurements on planar shock waves (velocity $\simeq 22$ km/s, pressure $\simeq 8$ Mbar) in solid aluminum which were generated by exposing a miniature sample to intense thermal x rays from a laser-heated cavity. The reflectivity of the free surface of the sample for the light from a probe laser ($\lambda = 532$ nm) and the absolute value of its optical emission were simultaneously registered with a 7-ps temporal resolution. For interpretation we used a two-temperature hydrodynamic code which includes the electron heat conduction and electron-ion relaxation and accounts for the nonequilibrium shock structure. The underlying self-consistent model for the equation of state and the transport coefficients of a metal over the relevant range of thermodynamic parameters are described in some detail. The reflectivity decay signal, which yields direct information on the effective collision frequency in the unloading material, and the emission peak, which is sensitive to the heat conductivity and dielectric permittivity of the hot and dense plasma behind the shock front, are well reproduced by the simulations. The emission signals are, however, longer than predicted, possibly due to the residual surface roughness in the experiment. On a longer time scale of 1–2 ns, the emission signal is well described by a simple radiation transport model with the Kramers-Unsöld opacity. [S1063-651X(97)09007-7]

PACS number(s): 52.25.Fi, 52.25.Mq, 52.25.Rv, 52.35.Tc

I. INTRODUCTION

Shock waves provide valuable information on the equation of state (EOS) of hot dense matter, which is required in many branches of applied and fundamental research [1]. An extensive and accurate database for EOS models in multimegabar region has been accumulated by measuring the shock velocity and particle speed behind the shock front [2,3]. It would, however, be of major importance to supplement these kinematic measurements by direct registration of the equilibrium temperature of the shocked material, at present a ''hidden'' parameter in many EOS models. A natural approach to its determination is via the optical radiation emitted by the shock-heated matter through the shock front towards the observer. An additional motivation to study optical emission from the shock waves is because it can provide information about the transport and relaxation phenomena in hot dense plasmas under the conditions not easily accessible in the laboratory.

The idea to use optical flashes that accompany the emergence of strong shocks at the free surface of an opaque metal was discussed long ago [1], but discarded as unpractical due to a very high temporal resolution ($\lesssim 1$ ps) required. Since then, the resolution of the optical diagnostics has improved significantly, and the problem was recently revisited and subject to a thorough theoretical scrutiny by Celliers and Ng [4]. Their conclusion was that, by measuring both the reflectivity and the emission of an emerging shock front on a time scale of 10–100 ps, one can (i) infer important information on the electrical conductivity of the unloading plasma and (ii) determine in a model-independent way the physical temperature of the emitting layer. Here we report the results of such measurements for an $\simeq 8$-Mbar shock wave in aluminum. Our experiments have been performed by using a technique of driving the shock waves in miniature samples with intense thermal x rays from a laser-heated cavity [5,6]. This technique ensures a very good quality of planar shock fronts and a negligible level of preheat ahead of the front.

To interpret the experimental results, we use two-temperature (2T) one-dimensional (1D) hydrodynamic simulations which account for the nonequilibrium structure of the shock front. Although the theoretical analysis by Celliers and Ng [4] was done in the one-temperature approximation, their experiments with silicon [7,8] have clearly demonstrated the need for a 2T model for interpretation of the optical signals from emerging shock waves. We have developed a relatively simple, partly phenomenological, but self-consistent model for the 2T equation of state and the transport coefficients of a metal over the relevant range of thermodynamic parameters. In doing so, our aim was not to create a new theoretical model as an alternative to others, but rather to get a flexible, self-consistent, and readily available theoretical framework, within which we would be able to analyze our data, test the sensitivity of the observed signals to the relevant physical quantities, and get a better feeling for the value of this type of experiments in exploring the properties of strongly coupled plasmas.

The structure of the paper is as follows. First, to gain insight into what could be measured under the ideal experimental conditions, we describe the theoretical model and analyze the spatial structure of the emerging shock front and the temporal structure of the optical signals (Sec. II). Then

*On leave from Institute for Theoretical and Experimental Physics, Moscow 117259, Russia.
†On leave from Troitsk Institute for Innovation and Fusion Research, Troitsk 142092, Moscow region, Russia.
‡On leave from Max-Planck-Institut für Quantenoptik, D-85748 Garching, Germany; Technische Hochschule Darmstadt, Germany.

the experimental setup and results are presented (Sec. III), followed by the interpretation of the observed reflectivity and emission signals (Sec. IV) and a summary (Sec. V).

II. THEORETICAL MODEL

To simulate the luminosity and reflectivity of a shock front emerging at a metal surface, we employ the free-electron model, which proved to be quite successful in explaining the thermal, electrical, and optical properties of metals near normal conditions [9]. In this approach, it is assumed that the electrical and thermal conductivities of a metal are due to a certain amount of free electrons which obey Fermi-Dirac statistics. The number z of free electrons per atom is defined as the degree of ionization. This approach merges naturally with the theory of ionized plasma states.

A. Equation of state and ionization equilibrium

The equation of state is an important ingredient in any model for interpreting the results of shock-wave experiments. The equation of state of aluminum is reasonably well known and available, for example, from the SESAME tables [10]. The main reason for constructing an EOS model of our own stems from the necessity to have a two-temperature EOS and calculate the degree of ionization $z=z(\rho,T_e)$ in a thermodynamically self-consistent way. Also, as contrasted to tabular forms of the EOS, a relatively simple model with several free parameters gives more flexibility in testing the sensitivity of the final results to the equation of state. In addition, we note that the model presented here can be accommodated to describe in a simple phenomenological way the insulator-metal phase transition and, consequently, applied to the analysis of pyrometric data for shock waves in insulators and semiconductors.

We assume that the total free energy is a sum of the cold, the thermal electron, and the thermal ion components,

$$F=F_c(\rho)+F_e(z,\rho,T_e)+F_i(\rho,T_i), \tag{1}$$

where ρ is the density and T_e and T_i are, respectively, the electron and ion temperatures. The cold pressure (from which one readily reconstructs F_c) of aluminum is approximated as

$$P_c(\rho)=\begin{cases} B\sigma^m(\sigma^n-1)/n, & \sigma<1, \\ B\sigma^2\ln\sigma, & \sigma>1, \end{cases} \tag{2}$$

where $\sigma=\rho/\rho_0$, ρ_0 is the normal density, and B is the bulk modulus; the parameters m and n are related to one another in such a way as to give the correct value of the cohesive energy. With $m=4/3$, $n=6.62$, and for $\sigma\lesssim 3$, Eq. (2) agrees to within a few percent with the SESAME cold curve of aluminum [10].

The electron component of the free energy is written in the form

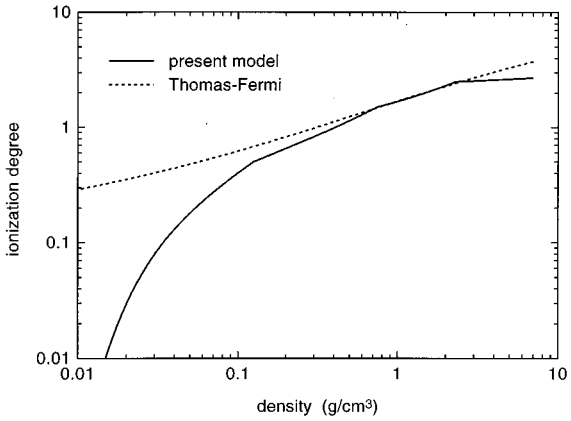

FIG. 1. Ionization degree of aluminum for a quasi-isentropic temperature-density profile $T_e=5\ \mathrm{eV}(\rho/7\ \mathrm{g\ cm^{-3}})^{0.5}$.

$$F_e(z,\rho,T_e)=-\frac{3}{2}zT_e\ln\left[1+\frac{2}{g_0}\frac{T_e}{(3\pi^2z\rho)^{2/3}}\right]+\int_{z_c}^{z}I(z)dz + \left(\frac{4\pi}{3}\rho\right)^{1/3}\left[\frac{1}{2}\beta(z_c^2-z^2)+z_0(z_c-z)\right], \tag{3}$$

where all dimensional quantities are in atomic units. This expression has three free parameters g_0, β, and z_0. For $g_0=6/\pi^2$, the first term in Eq. (3) is simply an analytic approximation to the thermal component of the free energy of Fermi-Dirac electrons. The second term is the ionization energy, and the third term stems from the ionization potential lowering, for which we assumed a simple form

$$\Delta I(z,\rho)=-\left(\frac{4\pi}{3}\rho\right)^{1/3}(\beta z+z_0), \tag{4}$$

inferred from an estimate for the screening effect by a uniform background of free electrons. Ionization potentials $I(z)$ are treated as a continuous function of z (for simplicity, we used the piecewise linear interpolation proposed by Raizer [11]). The degree of ionization z is calculated by solving the ionization equation $\partial F_e/\partial z=0$; $z_c=z_c(\rho)$ is the cold ionization degree at $T_e=0$. A fairly good agreement with the cold Thomas-Fermi ionization curve can be achieved with $\beta=0.8$–1.1. For aluminum, we used the values $\beta=0.8$, $z_0=1.2$, which, in particular, yield a cold ionization at normal density $z_c(\rho_0)=2.51$. As an illustrative example, Fig. 1 compares our values of z with those of the Thomas-Fermi model as calculated with the fit formula by More [12] for the temperature profile $T_e=5\ \mathrm{eV}(\rho/7\ \mathrm{g\ cm^{-3}})^{0.5}$, which approximates roughly the temperature-density dependence in the isentropic release wave behind a 10-Mbar shock in aluminum. The ''kinks'' along our curve are caused by the piecewise linear interpolation for the ionization potentials $I(z)$.

The ion component of the free energy is taken in the form

$$F_i(\rho,T_i)=\frac{3}{2}T_i\ln\frac{1+\lambda\Gamma_i}{T_i\rho^{-2/3}},\quad \Gamma_i=\left(\frac{4\pi}{3}\rho\right)^{1/3}\frac{z_{ci}^2(\rho)}{T_i}, \tag{5}$$

proposed originally by Kormer *et al.* [13]. Here, also, all quantities are in atomic units, λ is a fit parameter set equal to 0.1, and $z_{ci}(\rho)$ is a fit function related to the density dependence of the melting temperature. In our simulations, we used a simple approximation $z_{ci}=Z(1+3.5\rho_0/\rho)^{-1}$.

In this form, our EOS model reproduces quite accurately the experimental Hugoniot adiabat $P_H(\rho)$ of aluminum up to the pressures $P_H \simeq 15$ Mbar. If we choose the parameter g_0 (which controls the electron component of the heat capacity) to be equal to 0.2, we achieve a very good agreement with the SESAME tables for the values of the Hugoniot temperature as well.

B. Conductivity model

Adequate simulations of nonequilibrium shock fronts must take into account at least the following three effects [1,7,8]: (i) the electron heat conduction, (ii) the electron-ion (e-i) energy exchange, and (iii) the complex refractive index across all layers of the sample as a function of the light frequency ω (conductivity model).

The heat conduction and the e-i energy exchange determine the profile of the electron temperature across the shock front, whereas the conductivity model tells us what layer along this profile is seen by an observer. Because all these three effects are coupled to the same e-i collisions, our approach is to describe them within the same formalism. We use the same transport cross section $\sigma_{\rm tr}$ of e-i scattering to calculate the thermal conduction coefficient κ_{ei}, the e-i energy exchange coefficient χ_{ei}, and the complex dielectric permittivity $\varepsilon(\omega)$. The effects of strong ion-ion coupling are included into the expression for $\sigma_{\rm tr}$. Before applying our model to the shock-wave experiments, we check it against the known properties of aluminum near normal conditions.

In a weakly coupled plasma, the transport cross section is that of the Coulomb scattering [14]:

$$\sigma_{\rm tr}=\frac{4\pi z_i^2 e^4}{m^2 v^4} L_{ei}, \tag{6}$$

where m and v are, respectively, the electron mass and velocity, $+ez_i$ is the ion charge, and L_{ei} is the Coulomb logarithm with an appropriate cutoff for the minimum transferred momentum,

$$L_{ei}=\ln\Lambda_{ei}, \quad \Lambda_{ei}=\frac{2mv}{\hbar/D_{ei}}. \tag{7}$$

Here D_{ei} is the Debye radius defined by

$$D_{ei}^{-2}=D_e^{-2}+\frac{4\pi n_i z_i^2 e^2}{T_i}, \quad D_e^{-2}=\frac{4\pi n_e e^2}{[T_e^2+(\frac{2}{3}\epsilon_F)^2]^{1/2}}, \tag{8}$$

where n_i and n_e are, respectively, the number densities of ions and free electrons. In Eq. (7) we assumed the quantum value $\hbar/D_{ei}$ for the minimum transferred momentum. The latter is adequate for the high-velocity limit $\hbar v > e^2 z_i$ and never gets significantly below the classical value $e^2 z_i/vD_{ei}$ in situations of practical interest. In Eq. (8), the effect of electron degeneracy is taken into account as proposed in Ref. [15]; $\epsilon_F=\frac{1}{2}mv_F^2=\frac{1}{2}(\hbar^2/m)(3\pi^2 n_e)^{2/3}$ is the Fermi energy.

Turning now to the limit of strong ion-ion coupling, we note that the Coulomb divergence in the transport cross section for the e-i scattering does not occur when the ion-ion correlations are taken into account [16]. This indicates that the limit of strong ion-ion coupling could be included by modifying appropriately the Coulomb logarithm in Eq. (6). Our goal is to introduce such a modification for the case when the ion temperature T_i exceeds the Debye temperature T_D.

When $T_i > T_D$, the phonon gas in a crystal lattice can be treated as classical oscillations of individual ions in their local potential wells. The transport cross section for the electron scattering by one such ion can be evaluated as the Born cross section

$$\sigma_{\rm tr} \propto \frac{z_i^2 e^4 \xi^2}{\hbar^2 v^2} \tag{9}$$

for scattering on a dipole potential

$$U(r)=\frac{z_i e \xi}{r^2} \tag{10}$$

created by a thermal displacement

$$\xi \propto \left(\frac{T_i}{n_i z_i^2 e^2}\right)^{1/2} \tag{11}$$

of a lattice ion from its equilibrium position under the assumption that the free electrons form a uniform background of compensating negative charge [17]. Comparing Eq. (9) with Eq. (6), we conclude that the transport cross section in this limit, $\sigma_{\rm tr} \propto e^2 T_i/\hbar^2 v^2 n_i$, can be obtained directly from Eqs. (6)–(8) by assuming

$$L_{ei} \propto \Lambda_{ei}^2 \tag{12}$$

when $\Lambda_{ei} < 1$ and $T_i \lesssim [T_e^2+(\frac{2}{3}\epsilon_F)^2]^{1/2}$. The numerical factor in Eq. (12) is determined by the details of the phonon spectrum and Fermi surface of a given crystal, which is beyond the scope of our consideration. We match the two asymptotical forms of L_{ei} by adopting a simple interpolation formula

$$L_{ei}=\ln\left(1+\frac{\Lambda_{ei}}{1+g_{ei}/\Lambda_{ei}}\right). \tag{13}$$

This expression provides a smooth transition from the limit of a weakly coupled plasma [with $L_{ei}=\ln\Lambda_{ei}+O(\Lambda_{ei}^{-1})$ at $\Lambda_{ei} \gg 1$] to the limit of a solid metal at room temperature ($\Lambda_{ei} \ll 1$, $T_i > T_D$) and has one free parameter g_{ei}. The value of g_{ei} does not affect the limit of the weak ion-ion coupling, but can be chosen to fit the experimental conductivity and optical properties of a particular solid near the room temperature. The physical meaning of parameter g_{ei} is clarified by noting that, for a typical metal at normal conditions when $T_i = T_e \ll \epsilon_F$, the mean free path for the electron-phonon scattering, $l_{ei}=1/n_i\sigma_{\rm tr}=\frac{1}{4}g_{ei}(\hbar^2 v_F^2/e^2)/T_i$, is directly proportional to the value of g_{ei} and, in accordance with the theory of solids [9], inversely proportional to the lattice temperature T_i.

Given the transport cross section for the e-i scattering, we use the approximation of the Lorentz plasma to calculate the

required transport coefficients, similarly to how it was done by Lee and More [18]. In this case, the linearized Boltzmann equation for the distribution function of free electrons can be solved in the approximation of velocity-dependent collision frequency [14]. The effects of Fermi degeneracy are accounted for by using the Fermi-Dirac equilibrium distribution function $f_0(\mathbf{p})$ (normalized to the electron number density n_e) in corresponding integrals for the transport coefficients and dielectric permittivity. In particular, the complex dielectric permittivity at a frequency ω is given by [14]

$$\varepsilon(\omega)=1+4\pi e^2\int \frac{v^2}{3}\frac{(1-i\nu_{ei}/\omega)}{\omega^2+\nu_{ei}^2}\frac{\partial f_0}{\partial \epsilon}\,d^3\mathbf{p}, \quad (14)$$

where $\mathbf{p}=m\mathbf{v}$ and $\epsilon=\frac{1}{2}mv^2$ are, respectively, the momentum and the energy of a free electron, and $\nu_{ei}=\nu_{ei}(v)=n_i v\sigma_{\rm tr}$ is the velocity-dependent collision frequency. The electrical dc conductivity σ_{ei} is recovered from Eq. (14) in the limit $\omega\to 0$ through the relationship $\lim_{\omega\to 0}\mathrm{Im}[\varepsilon(\omega)]=4\pi\sigma_{ei}/\omega$. The heat conductivity κ_{ei} due to the e-i collisions is expressed in terms of similar integrals [14,18].

It is well known that, besides e-i collisions, the electron-electron collisions are also important for the heat conduction: They dominate in the limit of nondegenerate low-Z weakly coupled plasmas [19] and still play a significant role in moderately degenerate plasmas [20]. We take them into account in a simplified manner by using the Matthiessen rule

$$\kappa_e=(\kappa_{ei}^{-1}+\kappa_{ee}^{-1})^{-1} \quad (15)$$

and the following interpolation to the calculations by Lampe [20]:

$$\kappa_{ee}^{-1}=\frac{72}{5\pi^3}\frac{e^4}{T_e^2 v_F}\left[1+\left(\frac{T_e}{6\epsilon_F}\right)^2\right]^{-1/4}\frac{2}{3}\ln\left(1+\frac{\Lambda_{ee}^{3/2}}{1+0.12\Lambda_{ee}^{3/2}}\right), \quad (16)$$

$$\Lambda_{ee}=\frac{D_e}{\hbar}\frac{\sqrt{2mT_e}}{[1+(9\pi\epsilon_F/64T_e)^2]^{1/4}}. \quad (17)$$

Note that Λ_{ee} can be less than 1.

Figure 2 shows how our conductivity model compares with the tabulated experimental data [21] for aluminum at normal density. Plotted are three curves for three different values of the fit parameter g_{ei}. For simplicity, the ionization degree was fixed at $z=3$ for the entire temperature range of Fig. 2(a). As might be expected, no single value of parameter g_{ei} can fit perfectly both the optical and heat conductivity data. However, in the absence of a more accurate model for hot compressed metallic states, the accuracy of about a factor of 2–3 provided by our scheme should be acceptable, at least as the first step in our effort to interpret the experimental data.

C. Electron-ion temperature relaxation

In the case of weakly coupled Maxwellian plasmas, the rate of energy exchange between electrons and ions [14,19] can be expressed as

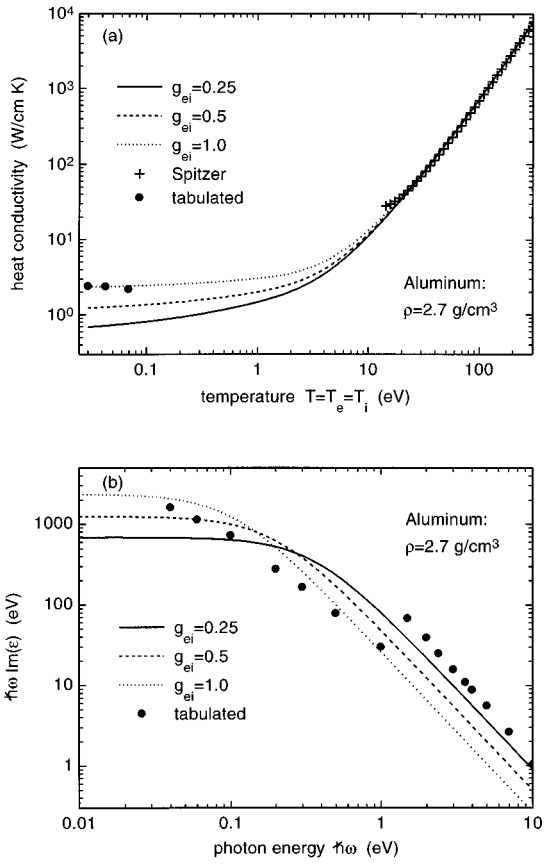

FIG. 2. (a) Temperature dependence of the heat conductivity of aluminum at normal density for three values of the fit parameter g_{ei}. (b) Imaginary part of the dielectric permittivity of aluminum at normal conditions as a function of the photon energy $\hbar\omega$. In both cases, the ionization degree was ''frozen'' at $z=z_i=3$. Solid circles show tabulated values from Ref. [21].

$$\rho\frac{d\epsilon_i}{dt}=-\rho\frac{d\epsilon_e}{dt}=3\frac{m}{m_i}n_e\langle\nu_{ei}\rangle(T_e-T_i)\equiv\chi_{ei}(T_e-T_i), \quad (18)$$

where ϵ_i and ϵ_e are, respectively, the specific internal energies of ions and electrons, m_i is the ion mass, and

$$\langle\nu_{ei}\rangle=\int \nu_{ei}v^2\frac{\partial f_0}{\partial\epsilon}\,d^3\mathbf{p}\Big/\int v^2\frac{\partial f_0}{\partial\epsilon}\,d^3\mathbf{p}. \quad (19)$$

is the mean collision frequency. Brysk [22] has demonstrated explicitly that exactly the same formula (18) is valid in the case of partially degenerate electrons, provided that the mean collision frequency (19) is calculated with the Fermi-Dirac distribution function $f_0(\mathbf{p})$.

In this work, we assume that the range of applicability of Eqs. (18) and (19) can be extended to the case of strongly coupled plasmas and hot metals (with ion temperatures T_i in excess of the Debye temperature T_D), provided that the effects of ion-ion correlations are accounted for when calculating the velocity-dependent collision frequency $\nu_{ei}=n_i v\sigma_{\rm tr}$. To corroborate such an assumption, the following arguments could be pointed out.

First of all, Eq. (18) is quite transparent from the point of view of energy and momentum conservation in binary collisions of free electrons with classically moving ions. Of course, a more rigorous treatment may change the numerical factor in Eq. (18), when the details of the phonon spectrum and the electron density of states in a particular metal are properly accounted for. In other words, a certain effective rather than the vacuum electron mass may enter Eq. (18). But in a shock-compressed and -heated metal, where the relevant energy of conduction electrons is relatively far from the bottom of the conduction zone, the effective electron mass is likely to approach its vacuum value m.

The experimental values of the e-i energy transfer rate measured recently in several metals [23–25] at room temperature, although sometimes controversial, fall in the range $\chi_{ei} \simeq 10^{16}-10^{17}$ W/m^3 K. Within the accuracy of about a factor of 3, these data are consistent with Eq. (18), provided that the collision frequency ν_{ei} is evaluated by applying the Drude formula to the tabulated values [21] of the complex refractive index for a corresponding metal at optical frequencies ($\hbar\omega \simeq 2.5$ eV).

Thus consistently with the overall accuracy of our approach to about a factor of 2–3, we expect Eq. (18) to be adequate for modelling the e-i temperature relaxation across multimegabar shock fronts in metals.

D. Numerical code

To simulate the propagation and breakout of a shock front, the above-described model was incorporated into the one-dimensional three-temperature Lagrangian hydrodynamic code DEIRA, developed originally for the purposes of inertial confinement fusion [26]. For the shock temperatures of interest here, the effect of radiative energy transport on the hydrodynamic motion is negligible. Hence we ignore energy transport by radiation when solving the hydrodynamic equations and calculate the shock luminosity by a postprocessor method. This is done by solving the Helmholtz wave equation [27] for the probe light of frequency $\omega = 2\pi c/\lambda$ with a given polarization, incident at a given angle on the snapshot structure of the sample taken from the hydrodynamic simulation. The optical properties of the sample are represented by the dielectric permittivity as given by Eq. (14). Such a calculation yields the total reflectivity and the absorption profile for the probe light. By virtue of Kirchhoff's law, the absorption profile is then multiplied by the local Planckian intensity $B_\lambda(T_e)$ and integrated over the sample thickness to yield the emission signal at a wavelength λ. A more detailed description of this procedure can be found in Ref. [4]. It takes automatically into account the reflection and absorption by all the target layers. All the calculations and measurements discussed in this paper have been done for the case of normal incidence, when no distinction should be made between the p- and s-polarized light.

E. Shock structure and temporal profiles of the optical signals

Figure 3 displays the structure of a 7.9-Mbar (22-km/s) shock front in aluminum as calculated with the model described above. It has the same basic features as the 2T shock front in a weakly coupled plasma [1]. Aluminum stays metallic both ahead and behind the shock front, with the ionization degree $z \simeq 3$ increasing only slightly across the density jump. Due to the electron heat conduction, a 200-nm-long precursor of the electron temperature is formed ahead of the density jump. The electron temperature in the precursor has a nearly exponential profile because the heat capacity and the heat conduction coefficient of degenerate electrons in the precursor zone are both directly proportional to T_e. In this case, the nonlinear heat conduction equation for T_e reduces to the classical linear one for T_e^2. Behind the density jump, an e-i temperature relaxation zone extends for some 20 nm. Note that the accuracy of our model in reproducing the length scales of the precursor and the relaxation zone should be about a factor of 2.

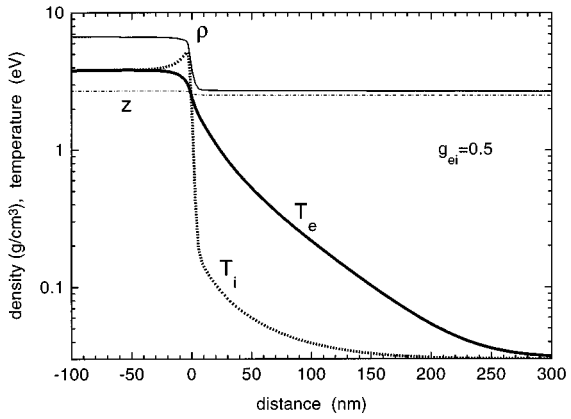

FIG. 3. Structure of a 7.9-Mbar (22-km/s) shock wave in aluminum as calculated for $g_{ei} = 0.5$.

Figure 4 shows the temporal structure of the emission and reflection signals at a wavelength $\lambda = 532$ nm for a 7.9-Mbar (22-km/s) shock wave emerging at a free surface of aluminum. The emission signal is presented in terms of the uncorrected, $T_{b,\mathrm{uncor}}$, and corrected, $T_{b,\mathrm{cor}}$, values of the brightness temperature defined as

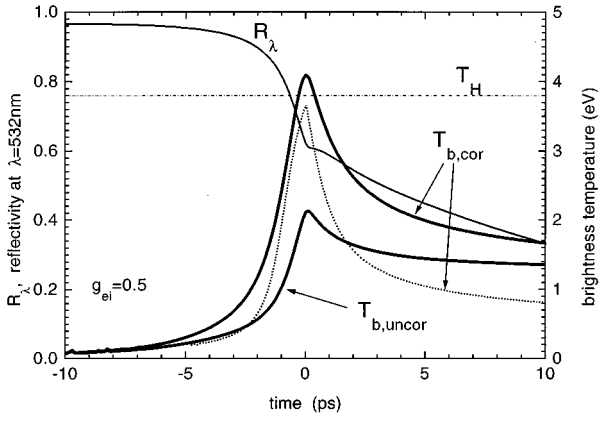

FIG. 4. Temporal behavior of the reflectivity R_λ and emission from a 7.9-Mbar (22-km/s) shock wave emerging at the surface of aluminum sample. The emission signal at the wavelength $\lambda = 532$ nm is presented in terms of the brightness temperature $T_{b,\mathrm{uncor}}$. Here $T_{b,\mathrm{cor}}$ is the brightness temperature corrected for the instantaneous value of the reflectivity. The narrow peak of emission (broken curve) was calculated with the equilibrium ($T_i = T_e$) steplike shock profile.

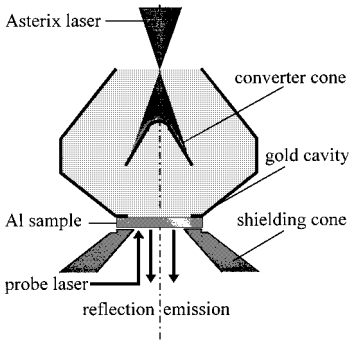

FIG. 5. Arrangement of the laser-heated cavity and a sample.

$$F_\lambda(t)=B_\lambda(T_{b,\mathrm{uncor}}), \tag{20}$$

$$F_\lambda(t)=[1-R_\lambda]B_\lambda(T_{b,\mathrm{cor}}), \tag{21}$$

where F_λ [W/cm^2 sr Å] is the spectral intensity of the shock emission at wavelength λ, R_λ is the reflection coefficient at the same wavelength λ, and $B_\lambda(T)$ is the Planckian intensity for temperature T. A considerable difference between the $T_{b,\mathrm{cor}}$ and $T_{b,\mathrm{uncor}}$ curves illustrates clearly that simultaneous measurements of the reflectivity and emission are required for determination of the Hugoniot temperature.

Reflectivity of the aluminum surface begins to fall some 3–5 ps before the shock arrival because the hot electrons in the thermal precursor heat up the ions and the e-i collision frequency increases in direct proportion with the ion temperature T_i. Reflectivity of the shock front itself, clearly visible as a ''kink'' on the R_λ curve, is about 60%. The emission signal exhibits a sharp peak at the time of shock arrival. When corrected for the instantaneous reflectivity value, the peak of the brightness temperature $T_{b,\mathrm{cor}}$ rises slightly above the Hugoniot temperature T_H. Such a transient overshooting of $T_{b,\mathrm{cor}}$ is caused by the interaction of the 2T shock front with the free boundary. Figure 4 shows that a temporal resolution of $\simeq 1$ ps (for a 20-km/s shock wave) is required to resolve the emission peak and the ''kink'' on the reflectivity curve.

The dashed $T_{b,\mathrm{cor}}$ curve in Fig. 4 shows the emission signal calculated in the equilibrium single-temperature ($T_e = T_i$) approximation for a steplike shock profile, with $\kappa_e = 0$ and $\chi_{ei}=\infty$. It exhibits a considerably more narrow peak and a more rapid decay than the nonequilibrium $T_{b,\mathrm{cor}}$ curve. When convolved with a broad [full width at half maximum (FWHM) $\gg 1$ ps] instrumental response function, the difference in the widths of the two peaks will be transformed into a considerable difference in their heights. From this we conclude that it is important to take into account the nonequilibrium shock structure when interpreting the emission signals from the shock fronts emerging at a free metal surface.

III. EXPERIMENT

A. Experimental setup

In our experiments intense shock waves were driven through aluminum samples by intense thermal x rays generated in a laser-heated cavity. A schematic view of the x-ray cavity and the sample is presented in Fig. 5.

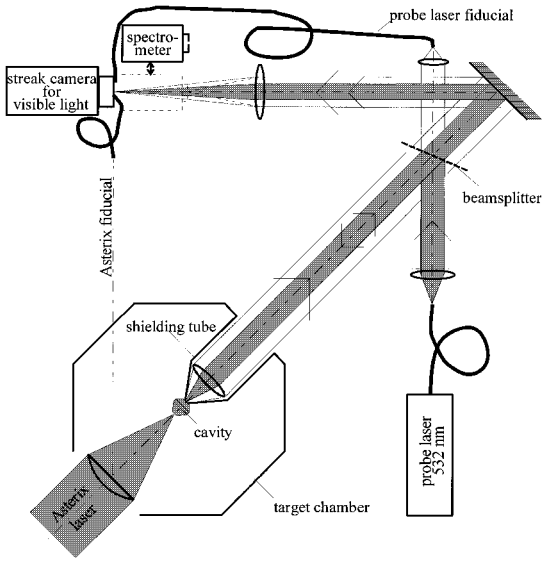

FIG. 6. Experimental setup.

The cavity was designed to achieve a uniform x-ray irradiation of the sample with a single laser beam. For this purpose, the sample is located on the axis of the cavity where the gradient of the radiation intensity is zero because of symmetry. The cavity is heated by the primary x rays, which originate on a laser-irradiated converter cone. In addition, the converter cone shields the sample against preheat by the primary x rays. The cavity case (diameter 1 mm) and the converter are made of gold. A more detailed description of the cavity and its properties will be given elsewhere [28]. The laser beam with a wavelength of 0.44 μm, an energy of up to 250 J, and a pulse duration of 450 ps is delivered by the iodine laser Asterix.

The samples were fabricated by diamond turning of massive aluminum. This process results in a root-mean-square surface roughness of less than 0.06 μm. Flat foils with a thickness of 20 μm and multistep foils with a step height of 7.5 μm were used. The sample and cavity were fixed with opaque glue on a shielding cone. Its aperture of 350 μm, somewhat smaller than the diameter of the heated area of the sample, limited the field of view for the reflection and emission measurements performed on the outer surface of the sample. The unit consisting of the cavity, the sample, and the cone was replaced as a whole after each shot.

A schematic overview of the experimental setup is given in Fig. 6. A light-tight metallic shielding tube holds at its tip the shielding cone with the sample the and cavity in the center of the target chamber; it allows the cavity to be adjusted with an accuracy of better than 10 μm in three directions relative to the fixed position of the laser focal spot. The shielding tube contains also an imaging objective ($f/2$, $F = 100$ mm), in which an exchangeable planar glass plate, serving as the debris shield and vacuum window, is integrated.

The sample is imaged (the light path being folded by a mirror) with the help of a second objective at a ten-fold magnification onto the entrance slit of the Hadland Imacon 500 streak camera. When the spectrograph shown in Fig. 6 is removed, the camera registers optical signals from the sample with the spatial and temporal resolution.

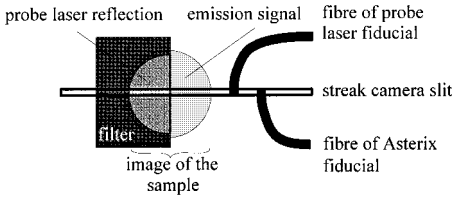

FIG. 7. Details of the arrangement of the filtered sample image and the optical fibers along the streak slit.

The light source for reflectivity measurements is a frequency-doubled Nd:YAG probe laser. It emits pulses of 6 ns duration at a wavelength $\lambda = 532$ nm. A beam splitter with 50% transmission couples the probe laser to the imaging system. The temporal shape is registered with the help of the probe laser fiducial. To generate this fiducial, laser light transmitted through the beam splitter is picked up by an optical fiber and guided to the streak slit. Another fiber picks up the light from the Asterix laser (as shown schematically in Fig. 6) and generates the Asterix fiducial. This fiducial provides the timing of the events relative to the Asterix pulse (the folding of the optical path by the mirror shown in Fig. 2 is necessary for the fiducial to reach the streak slit in time). Note that the fiducial is delayed by 560 ps on the streak photographs in order to record it together with the shock signal in the time window of the streak camera.

The optical technique used to register the reflection and emission signals is illustrated in more detail in Fig. 7. This figure shows the position of the sample image and of the two optical fibers along the streak slit. Self-emission is measured from one half of the sample. The other half, where the self-emission is suppressed by a 2.5% transmission filter, is used to measure the reflectivity of the sample. It is only this other half which is irradiated by the probe laser. This is accomplished by imaging onto the sample a circular laser-illuminated diaphragm, one half of which is masked by an opaque screen. The required high-contrast, high-resolution image of the diaphragm on the sample was generated by an objective identical to that used for imaging the sample onto the streak camera. The half-masked diaphragm was illuminated with an optical fiber (see Fig. 6), which provided the appropriate temporal delay and, in addition, improved the spatial uniformity of the irradiation and smoothed the temporal fluctuations of the probe laser.

With the grating spectrometer (150 lines/mm grating, $F = 250$ mm focal length) inserted in front of the streak camera, the sample is imaged onto the plane of the entrance slit of the spectrometer with a 2.5-fold magnification and then by the spectrometer onto the plane of the entrance slit of the streak camera where the spectrum is registered. The spectrometer is operated with the entrance slit wider than the sample image, and the latter determines the spectral resolution. The dispersion direction of the spectrometer is oriented parallel to the streak slit. In this mode of operation the camera registers a spatial average of the sample emission with temporal and spectral resolution.

B. Temporal resolution and absolute calibration of the optical setup

The temporal resolution of the whole setup was tested by using a white-light continuum of sub-ps duration. It was generated by focusing an ~200-fs pulse from a Ti:sapphire laser into a 3-mm-thick sheet of fused silica, which replaced for this purpose the shock sample in the experimental chamber. A FWHM of 7 ps was measured for the response function of the whole setup at the wavelength of $\lambda = 532$ nm that is used for comparison with the theoretical model. The response function is presented in Fig. 10 below.

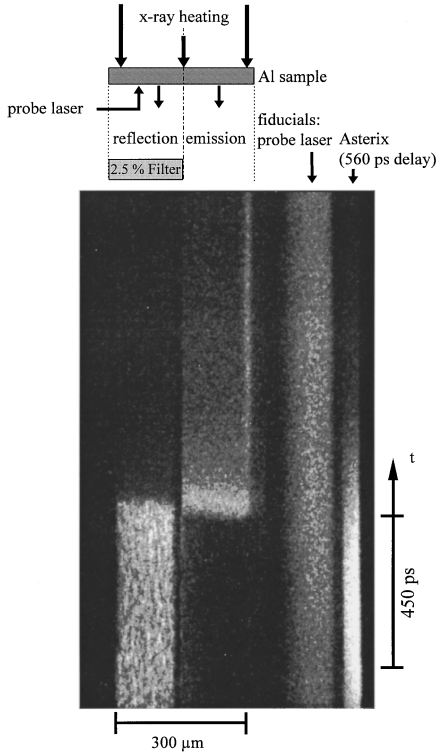

FIG. 8. Spatially resolved streak photograph obtained with a flat 20-μm-thick aluminum sample.

The comparison between the experiment and simulations is made by using the absolute fluxes. For the experimental determination of the emitted spectral flux F_λ the optical setup, including the spectrometer, was absolutely calibrated. The calibration was carried out at the wavelength $\lambda = 532$ nm with the help of the probe laser by injecting a known amount of laser light through the opening of the shielding cone into the detection system. The advantage of using a strong laser source is that the calibration can be carried out with the actual setup and with the camera operating in the streak mode. The accuracy of the calibration is estimated to be $\pm 7\%$. More details on the calibration procedure are given in Appendix A.

C. Experimental results

A spatially resolved streak photograph (i.e., one taken without the spectrograph) obtained in an experiment with a 20-μm-thick flat aluminum sample is shown in Fig. 8. Despite the miniature size of the sample, the traces corresponding to the reflected laser light to the emission signal and to the two fiducials are very clearly resolved in the spatial (horizontal) direction. In the temporal direction, the shock arrival is indicated by a sudden drop to zero of the reflected laser intensity. This drop is accompanied by a simultaneous rise in

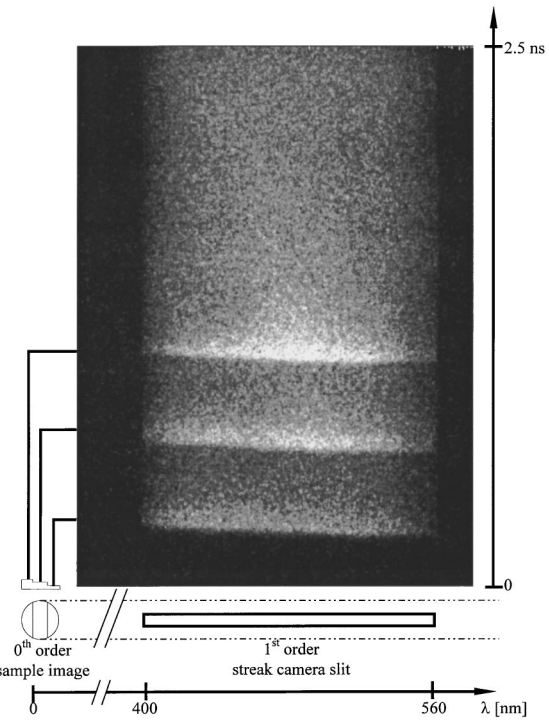

FIG. 9. Spectrally resolved streak photograph obtained with a two-step aluminum sample.

the emission from the sample. The emission signal then decays as the shock-heated material expands and cools.

For a planar shock wave aligned parallel to the sample surface, the temporal profiles of the reflection and emission signals should not vary along the spatial (horizontal) direction. This synchronism is indeed observed in the experiment shown in Fig. 8. However, it was found to depend critically on careful alignment of the cavity with respect to the heating laser beam and on the quality of the samples, which, in particular, had to be free of dust and scratches.

It should be emphasized that, due to the simultaneous measurement of the reflectivity and emission, the experiment provides an accurate relative timing between the two signals. The reflectivity is obtained as the ratio of the reflected signal to the probe laser fiducial after calibration against a sample of known reflectivity. The main source of noise in the reflectivity measurements are speckles in the reflected laser light (as is seen in Fig. 8). They arise in the process of imaging with coherent laser light.

With the grating spectrometer inserted into the optical setup, streak photographs of the type shown in Fig. 9 have been obtained. The length of the streak slit determines the spectral range from 400 to 560 nm. A two-step aluminum sample was used in this particular experiment. Each time the shock breaks out at one of the three thickness levels of the sample, a spectrally and temporally resolved flash of light is recorded by the camera. With the known step thickness and the time delay between successive flashes, we determined the shock speed of 22 ± 0.5 km/s and measured the absolute spectral emission flux F_λ with the peak value of 9.2 ± 0.7 W/cm^2 sr Å. The spectral resolution is determined by the step width and was about 80 Å in this experiment. It may be noted that the flashes of light are slightly inclined with respect to the horizontal axis. This effect is due to the dispersion in the optical setup and was reproduced with the white-light continuum test source as well.

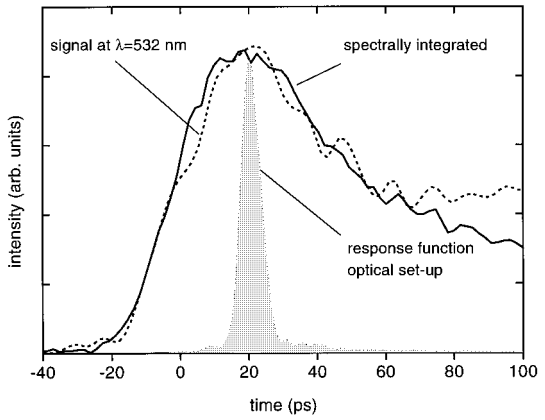

FIG. 10. Temporal shape of the spectral flux at 532 nm and of the spectrally integrated flux. Also shown is the response function of the optical setup measured at $\lambda = 532$ nm by using a laser-generated sub-ps white-light continuum.

It is the spectral flux F_λ at $\lambda = 532$ nm as a function of time that we compare with simulations in the next section. Analysis of the spectrally resolved streak photographs showed that the temporal profile of F_λ is virtually independent of the wavelength λ over the measured spectral range and practically identical with the profile of the spectrally integrated emission (the estimated effect of the dispersion on the width of the spectrally integrated emission is consistent with this result). This is illustrated in Fig. 10 with the plots of the spectrally integrated flux and the spectral flux at 532 nm made from the streak images shown in Figs. 8 and 9, respectively. Hence we can assign the absolutely measured scale of F_λ (at 532 nm) to the spectrally integrated emission signal (as measured without spectrometer) and use the latter to compare with the model simulations (see Fig. 11 below). Because the spectrally integrated signal has been measured simultaneously with the reflectivity, such a procedure reduces playground for comparison between theory and observations.

IV. INTERPRETATION OF THE EXPERIMENTAL RESULTS

Figure 11 shows the measured reflectivity R_λ and emission F_λ [W/cm^2 sr Å], signals for the 7.9-Mbar (22-km/s) shock wave together with two theoretical curves for each signal. The latter were convolved with a Gaussian of FWHM equal to 7 ps. In this way the temporal resolution of the streak camera is taken into account. In simulations, time $t = 0$ is defined as the time of shock arrival at the free surface. For the experimental R_λ and F_λ curves, there is a freedom in choosing the reference point along the time axis as to achieve the best agreement with the simulations. We used this freedom to place the experimental R_λ curve on top of the dashed theoretical R_λ curve.

As may be seen in Fig. 11, the shapes of the measured and calculated R_λ curves are close to each other. The measured emission F_λ signal, however, rises noticeably slower (on a time scale of 25–30 ps) and has a broader peak (which is also delayed by some 10–15 ps) than the theoretical curves,

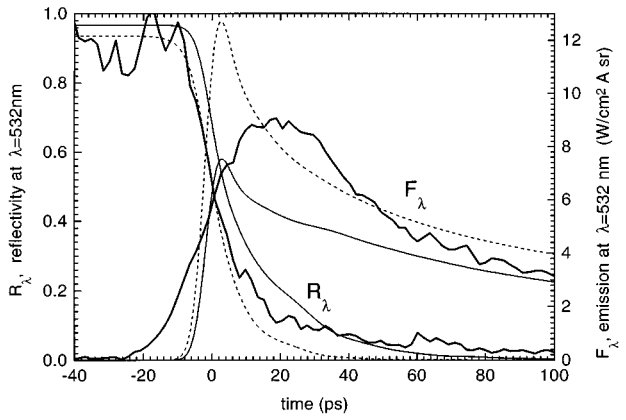

FIG. 11. Measured reflectivity R_λ and spectral brightness F_λ at $\lambda = 532$ nm of the 22-km/s shock wave emerging at $t=0$ at the aluminum surface (thick solid curves). Theoretical (thin solid and dashed) curves have been calculated for $g_{ei}=0.5$. The dashed curves have been obtained with a doubled value of the electron heat conductivity κ_e and a doubled collision frequency ν_{ei} in Eq. (14) for the dielectric permittivity.

which already include the effect of the camera resolution. We proceed now to a detailed comparison between the experimental and theoretical results.

A. Reflectivity decay

The time scale of decay of the reflectivity signal R_λ offers a direct test for the conductivity model. Our measurements clearly indicate that, after the shock arrival, the reflectivity of the aluminum surface at $\lambda = 532$ nm drops from its initial value of $R_\lambda \gtrsim 90\%$ to less than 10% within the time interval of $t_{Rd} \lesssim 30$ ps. Note that this decay time is considerably (by at least a factor of 3) shorter than that measured by Ng *et al.* [29] for the same shock speed, but under the conditions of direct drive by the laser pulse.

For the sake of the present argument, we can assume that the time scale of the reflectivity decay is

$$t_{Rd} \propto \frac{c}{c_s \nu_{ei}}, \tag{22}$$

where c is the velocity of light, c_s is the sound speed behind the shock front, and ν_{ei} is a characteristic value of the collision frequency in the vicinity of the critical point $\omega = \omega_p$ (ω_p is the plasma frequency) along the electron density profile in the release wave. Equation (22) represents a rigorous result in the WKB approximation for the case of self-similar expansion of a given density profile, when the reflectivity is proportional to $\exp(-\alpha \nu_{ei} L/c)$ [30]. Here α is a constant characterizing the density profile and $L = c_s t$ is its length scale. Because the uncertainty in the value of c_s (due to the uncertainty in the EOS) is relatively small, the measured value of t_{Rd} provides—as one readily sees from Eq. (22)—an effective lower bound on the collision frequency ν_{ei} that enters the conductivity model. When we calculate R_λ more accurately by solving numerically the Helmholtz wave equation, we find that this lower bound can be established to an accuracy of a factor of 2–3 and is consistent with our conductivity model, based on the Drude-Boltzmann formalism, for the same values of the fit parameter $g_{ei} \simeq 0.2-0.5$, which provide close to the best agreement with the room temperature conductivity of aluminum. If, for example, we try to decrease artificially the collision frequency in the strongly coupled limit by increasing the value of the fit parameter to $g_{ei} \gtrsim 3-10$, we arrive at a sharp disagreement with the reflectivity measurements.

B. Shock emission

In contrast to the decay time of the reflectivity, the peak value of the emission signal is virtually insensitive to the value of the e-i collision frequency, provided that the same transport cross section is used to calculate the electrical and thermal conductivities and the e-i energy transfer rate. Hence, by analyzing the emission peak, we can gain additional information on the transport and relaxation phenomena which complements the information obtained from the reflectivity data.

The weak dependence of the peak emission level on ν_{ei} is explained by the following scaling law for the two-temperature shock waves: The equations governing the structure of a 2T shock front with electron heat conduction are invariant with respect to the scaling

$$\kappa_e \to \kappa_e Y^{-1}, \quad \chi_{ei} \to \chi_{ei} Y, \quad x \to x Y^{-1}, \tag{23}$$

where κ_e is the electron heat conduction coefficient, χ_{ei} is the e-i temperature coupling constant, and x is the coordinate across the shock front. In particular, the value of the electron temperature at the density discontinuity remains invariant when the collision frequency ν_{ei} is multiplied by an arbitrary scale factor Y, which implies the first two transformations in Eq. (23).

The emission peak is, however, sensitive to the relative weights with which ν_{ei} contributes to κ_e and χ_{ei} and allows us to test this aspect of the theoretical model. As already discussed in Sec. II B, the accuracy of our model in reproducing the values of κ_e and $\mathrm{Im}[\varepsilon(\omega)]$ in the strongly coupled limit is about a factor of 2. To exhibit this fact explicitly, two pairs of theoretical curves are plotted in Fig. 11. The thin solid R_λ and F_λ curves are in a sense the base-line theoretical signals, calculated with the equations of Sec. II for $g_{ei} = 0.5$. The dashed curves have been obtained from the solid ones by doubling both the value of κ_e and the contribution of ν_{ei} to $\varepsilon(\omega)$ in the Drude formula (14). As can be seen in Fig. 2, these are the ''fudge'' factors that bring the model into a better agreement with the room-temperature properties of aluminum. Clearly, the difference between the solid and the dashed theoretical curves represents the intrinsic inaccuracy of our model in predicting the R_λ and F_λ optical signals.

Within this uncertainty, the observed and the calculated peak values of F_λ, smoothed with the camera resolution, agree with each other. In its decay phase from 50 to 100 ps, the measured signal falls within the ''error bars'' of our theoretical model. Also, the area under the calculated dashed curve, i.e., the amount of light in the peak, agrees with the experiment.

We conclude that, within its limits, the self-consistent scheme for calculating the transport and relaxation coefficients of the shock-compressed aluminum based on the equa-

tions of Secs. II B and II C predicts correctly the intensity and the amount of light emitted upon the shock breakout.

C. Temporal profile of the emission signal

As already noted at the beginning of this section, the measured emission signal rises slower and has a broader peak than the theoretical curves.

When compared with the measured temporal response function of the optical detection system shown in Fig. 10, the variation of the observed flux appears to be slow enough to conclude that we have registered a ''true'' emission profile rather than the one smeared by the camera resolution. Thus, a major discrepancy between the present experiment and the theoretical predictions is the rise time and the shape of the peak of the emission signal. Note that for the reflectivity signal R_λ the situation is different. Within the limits set by the camera resolution, this signal does not show any indication for a slower than expected rate of decay.

The observation that the emission peak is significantly broader than the predicted one points towards a deficit either in the experiment or in the modelling. Let us first consider the possibility that the experiment has not reached yet the ideal case assumed in simulations. In this last context, it is enlightening to review briefly the earlier work performed elsewhere and the experience gained in our laboratory concerning the quality of the experimental data.

We note that the optical signals measured earlier from the shock waves driven by direct laser irradiation [29,7] displayed considerably slower decay time scales than in our present experiment. Our own direct-drive experiments (see Fig. 2 in Ref. [6]) have fully confirmed this fact. In our attempts to reach a new level of experimental quality, the following steps have been undertaken.

(i) *Nonplanar distortions of the shock front* have virtually been eliminated by incoherent x-ray drive.

(ii) *Preheating* of the sample, whose smearing effect on the emission peak is comparable to that observed in direct-drive experiments (see Fig. 3 in Ref. [6]), was suppressed by appropriate cavity design. For the present cavity and drive conditions, it was recently verified that $\gtrsim 20$-μm-thick silicon foils were preheated to less than 200 K. For aluminum, whose atomic number differs by only one, conditions should be similar.

(iii) *Surface roughness* was reduced to a 60-nm root-mean-square (rms) level by using diamond-turned samples. Test experiments with 5-μm-thick gold foils that were rough on one side (~ 1 μm rms) have shown a dramatic smearing effect when the shock front emerged on the rough side.

We believe that in the present experiment the causes (i) and (ii) can be excluded. There remains a possibility that the observed smearing of emission is caused by the surface roughness. On the one hand, the shock transit time across the 60-nm rugged surface layer is rather short, ~ 3 ps. On the other hand, a three-dimensional hydrodynamic flow develops when the shock front reaches the troughs on the rugged surface. Simple estimates show that hydrodynamic effects can enhance by a factor of ~ 2 the initial surface unevenness, and the emitting layer can retain the imprints of the ~ 60 nm initial roughness for a few tens of picoseconds.

To clarify the role of surface roughness, we conducted comparative experiments using gold foils with a much smoother surface than that of the diamond turned aluminum foils regularly employed in our experiments. The gold foils were produced by electroplating gold onto the surface of a silicon wafer. After peeling off the foil, the surface previously attached to the silicon was scanned by an atomic force microscope. The rms roughness was found to be only 1 nm, i.e., about 60 times less than for the aluminum foils. Shock breakout on this same surface under our standard drive conditions resulted in emission signals very similar to those observed with the aluminum foils. In fact, the rise time was slightly slower, as one might expect due to the reduced shock speed in gold. Hence these tests do not support the suggestion that the surface roughness was the cause for the broader than expected emission peak. It is of course possible that still other experimental deficits, which remained undetected despite our considerable efforts, cause the broader than expected emission signals. If they could be identified and eliminated, one would expect that the experimental signal should approach more closely the simulation results, smoothed by the given experimental temporal resolution.

The other possibility is that the experiment is already clean, and the cause for the discrepancy must be sought in the modeling. In this case the discrepancy should be considered as being between the measured signal and the unsmoothed simulation result (the experimental signal obtained with a camera of infinite resolution would be the same). It reduces basically to a much shorter predicted rise time and a narrow (~ 2 ps wide; see Fig. 4) spike of light at $t=0$ on top of each theoretical curve in Fig. 11 with a peak value 2 times higher than shown presently. It is possible that some unrecognized physical effect is operating, which smears the emission peak, or some essential ingredient is missing in our theoretical model. However, our experience with 1D simulations is that this discrepancy cannot be explained within the plain-parallel geometry, by simply modifying the transport and relaxation coefficients.

The simulation shown in Fig. 4 suggests that the Hugoniot temperature may in principle be determined using Kirchhoff's law (as originally proposed in Ref. [4]) from an expected kink of R_λ and the peak of F_λ at the shock breakout. Clearly, this possibility is not feasible at present, and not only because the required resolution of $\simeq 1$ ps has not yet been achieved, but also because the physical cause of the broader observed than predicted emission peak has not been clarified.

D. Long-term decay of emission

Optical emission of the unloading aluminum plasma in our experiments was measured over the total time interval of 1–2 ns. As is discussed in detail in Ref. [1], the long-term tail of the emission signal could be used to test the EOS model, provided that the opacity mechanism is known. At this stage, the reflectivity of the unloading layer can be neglected and, instead of solving the Helmholtz wave equation, one can employ the usual formalism of radiation transport to evaluate the observed flux F_λ (for more details see Appendix B).

Figure 12 compares the measured emission at $\lambda = 532$ nm with two theoretical curves calculated by combining the Kramers-Unsöld opacity formula [1] with the SESAME

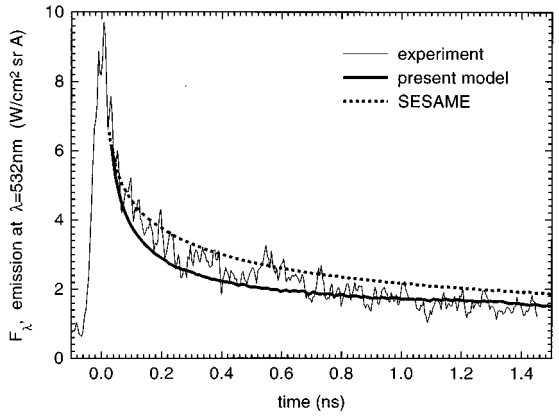

FIG. 12. Long-term behavior of the emission signal from the 22-km/s shock wave emerging at aluminum surface. Theoretical curves have been calculated by applying the Kramers-Unsöld formula in combination with the present (solid line) and SESAME (dashed line) EOS models.

and the present EOS models. Both theoretical curves agree well with the observations. The latter implies that the observed long-term behavior of the emission signal is fully compatible with the both EOS models and with the Kramers-Unsöld opacity formula. We cannot, however, make any stronger statement in the sense that our measurements confirm a particular EOS model because the applicability of the Kramers-Unsöld opacity formula, at times as short as 1–2 ns, is highly questionable, and the agreement between theory and experiment demonstrated by Fig. 12 might be simply fortuitous. A more detailed discussion of this issue is presented in Appendix B.

V. SUMMARY

We have performed simultaneous optical measurements of the reflectivity R_λ and absolute emission F_λ at the wavelength $\lambda = 532$ nm from the unloading dense plasma behind a strong ($\simeq 8-$Mbar) shock wave in aluminum. To drive a high-quality planar shock front, we used a specially designed x-ray hohlraum heated to an effective temperature of 100–120 eV by a single 250-J (3ω) beam of the iodine Asterix laser. The shock speed $D = 22 \pm 0.5$ km/s was measured by using a two-step aluminum foil. To the best of our knowledge, we have achieved the highest temporal resolution so far in measuring the shock-breakout signals under well-controlled conditions in the multimegabar pressure range.

Our interpretation of the experimental data is based on the two-temperature (electron and ion) hydrodynamic modeling of the nonequilibrium structure of the shock front and the release wave. We have employed a relatively simple semiempirical self-consistent model, which provides within a common framework the thermodynamic, optical, and transport data. The equation of state has been calibrated against the SESAME Hugoniot curve of aluminum. The conductivity part of the model is based on the Drude-Boltzmann formalism and provides a smooth interpolation from the limit of the ideal plasma to the metal at room temperature.

The measurements of the reflectivity decay profile of the unloading aluminum surface offer a direct test for the conductivity model. Our data indicate the decay time of $t_{Rd} \lesssim 30$ ps. It implies a lower bound for the effective collision frequency which is fully consistent with the conductivity model used in simulations.

Our simulations indicate that the peak value of the optical emission after the shock release is rather sensitive to the heat conductivity and dielectric permittivity of the hot dense plasma behind the shock front. This makes the interpretation of the emission signals more involved and model dependent. Within the intrinsic uncertainty of our model, which is at least a factor of 2 for the values of the transport and relaxation coefficients, we find a fairly good agreement between the observed and calculated intensity and amount of light in the peak of the emission signal. The long-term (on the time scale of 1–2 ns) decay of the emission signal is consistent with the Kramers-Unsöld opacity model combined with the SESAME or the present equation of state.

An unexpected observation was that the rise time and the width of the emission peak were not as short as indicated by the simulations. All plausible candidates, like the limited time resolution, drive nonuniformity, sample preheat, and sample roughness, are most likely not responsible for this behavior. Nor does it seem possible to match the observations by variations of the transport coefficients within a 1D model. Only further investigations can show whether hitherto unrecognized physical effects determine the fine structure of the investigated shock waves.

ACKNOWLEDGMENTS

We would like to acknowledge many stimulating discussions with S. I. Anisimov and A. Ng, and the experimental support through scanning of gold samples with the atomic force microscope by W. Krieger and E. Soergel. This work was supported in part by the Bundesministerium für Forschung und Technologie (Bonn), by the commission of the European Communities in the framework of the Euratom-IPP Association, by the EC network High Energy Density in Matter (Contract No. ERB CT 930327), by INTAS-94-1105, and by HCM LSF-program EPB CHGE CT920006.

APPENDIX A: ABSOLUTE MEASUREMENT OF THE EMITTED SPECTRAL FLUX

The digital readout system of the streak camera subdivides the temporal axis into pixels of temporal width Δt_p and gives a signal S as the number of counts for each pixel. In the calibration process the laser energy ϵ transmitted through the opening with surface area A of the shielding cone into the objective is measured by a calorimeter. After insertion of a filter with transmission ϑ, the sum Σ of the total number of counts in all pixels (which corresponds to the injected laser energy) is determined. One obtains then the energy per count $\epsilon^* = \epsilon\vartheta/A\Sigma$. The width $\Delta\lambda_p$ of the (approximately rectangular) response function of the grating spectrometer for the monochromatic laser radiation is also measured. With Ω_l denoting the solid angle of the imaging objective and φ_s the ratio of the streak speeds of experiment and calibration, the value of the spectral flux F_λ (energy per unit time per unit area per unit solid angle per unit spectral interval) corresponding to a given signal S is given by

$$F_\lambda = \frac{\epsilon^*}{\Omega_l \Delta\lambda_p (\Delta t_p/\varphi_s)} S = \frac{e\vartheta/A\Sigma}{\Omega_l \Delta\lambda_p (\Delta t_p/\varphi_s)} S. \quad \text{(A1)}$$

The quantities which enter this formula can be readily measured with high accuracy.

APPENDIX B: LONG-TERM DECAY OF EMISSION IN TERMS OF THE KRAMERS-UNSÖLD MODEL

A certain time after the shock release, when the refraction index of the unloading plasma approaches unity, the optical brightness of the expanding layer can be evaluated by using the equation of radiation transport as

$$F_\lambda = \int_0^\infty B_\lambda(T_e(x)) \exp\left(- \int_0^x k_\lambda dx' \right) k_\lambda dx, \quad \text{(B1)}$$

where $k_\lambda = k_\lambda(x)$ is the absorption coefficient at wavelength λ. Zel'dovich and Raizer [1] proposed to use the Kramers-Unsöld formula

$$k_\lambda[\mathrm{cm}^{-1}] = 4.4\times 10^8 \frac{\rho T_e}{A(\hbar\omega)^3} \exp\left(- \frac{I_1 - \hbar\omega}{T_e} \right) \quad \text{(B2)}$$

to evaluate k_λ. This formula accounts for the free-free (e-i collisions) and free-bound transitions in a weakly ionized ($z \ll 1$) monoatomic vapour for photon energies $\hbar\omega \ll I_1$, where I_1 (5.99 eV for aluminum) is the first ionization potential. The numerical coefficient in Eq. (B2) applies when T_e and $\hbar\omega$ are in electron volts, and ρ is in g/cm^3. A major advantage of the Kramers-Unsöld formula is that it can be applied without calculating the ionization equilibrium and, as a consequence, combined with a wide variety of the EOS models. The spectral flux calculated with Eqs. (B1) and (B2) for the release wave behind a 22-km/s shock wave in aluminum by using the SESAME and the present EOS models is shown in Fig. 12.

Before drawing conclusions from comparison between the calculated and measured fluxes in Fig. 12, the conditions for applicability of the Kramers-Unsöld model should be examined. In our case, with the observations extending to only $t \simeq 1.5$ ns, these conditions may still be not satisfied. Qualitatively, this situation is illustrated in Fig. 13 for $t = 100$ ps. Here the thick dashed curve shows the Kramers-Unsöld absorption profile for $\lambda = 532$ nm. By virtue of the Kirchhoff's law, this profile represents the fraction of the local Planckian intensity received by a distant observer from a unit depth of the release wave. There are two main conditions that must be fulfilled for the Kramers-Unsöld model to be applicable: (i) the ionization degree z must be below unity, and (ii) the local plasma frequency ω_p must be smaller than the probe light frequency $\omega = 2\pi c/\lambda$ in the layer from where most of the emission originates. In Fig. 13 the Drude absorption profile calculated by solving the Helmholtz wave equation, which is localized around the $\omega = \omega_p$ surface, lies outward with respect to the Kramers-Unsöld profile. The latter means that the radiation flux calculated with Eqs. (B1) and (B2) cannot really propagate through matter and reach a distant observer. However, because both absorption profiles lie in the region of a nearly isothermal corona, they both yield nearly the same value of the emission flux F_λ. The formation of the isothermal corona in the rarefaction wave is due to the electron heat conduction during the first few picoseconds of expansion; it has been analyzed in detail by Celliers and Ng [4] and is unambiguously reproduced in our simulations.

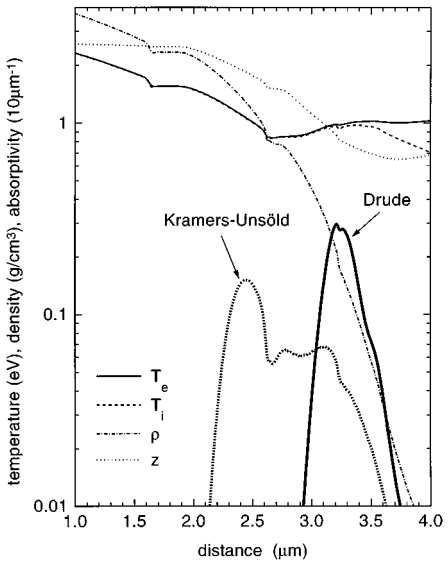

FIG. 13. Spatial profiles of density, electron, and ion temperatures, and ionization degree in the rarefaction wave behind the 7.9-Mbar (22-km/s) shock at $t = 100$ ps after the release. The ''kinks'' along these curves are caused by the piecewise interpolation of the ionization potentials $I(z)$ in Eq. (3) and bear no physical significance. Plotted also are the absorption profiles at $\lambda = 532$ nm calculated with the Drude (thick solid line) and Kramers-Unsöld (thick dashed line) models.

The time t_{KU}, after which the Kramers-Unsöld formula becomes applicable, is rather sensitive to the model used to calculate the ionization equilibrium. This is illustrated in Fig. 14, which shows the temporal variation of the ionization degree $z_{0.7}$ and ratio $(\omega/\omega_p)_{0.7}$ at the Kramers-Unsöld optical depth $\tau_{\mathrm{KU}} = 0.7$ for $\lambda = 532$ nm. The value $\tau_{\mathrm{KU}} = 0.7$ corresponds to a layer from which one-half of the total emission

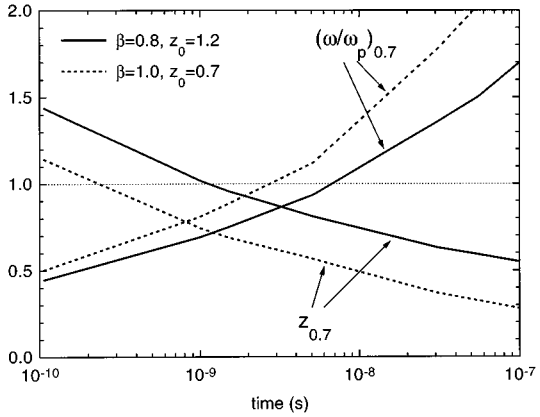

FIG. 14. Temporal behavior of the ionization degree $z_{0.7}$ and the ratio $(\omega/\omega_p)_{0.7}$ calculated in the layer where the Kramers-Unsöld optical depth $\tau_{\mathrm{KU}} = 0.7$ for $\lambda = 2\pi c/\omega = 532$ nm; ω_p is the local plasma frequency. Solid and dashed curves correspond to two different combinations of parameters β and z_0 in our EOS model.

would originate in the isothermal case. Two pairs of curves have been calculated for two different combinations of β and z_0 parameters in our EOS model [see Eq. (3)], which produce practically indistinguishable Hugoniot states, but yield different values of z along the release profile. From Fig. 14 we infer that the time t_{KU}, after which both $z_{0.7}<1$ and $(\omega/\omega_p)_{0.7}>1$, lies in the range $t_{\mathrm{KU}}\simeq 1-10$ ns.

Figure 12 displays a fairly good agreement between the observed and the calculated Kramers-Unsöld emission signals on the time scale of 1.5 ns. This agreement, however, cannot be considered as an evidence favoring one of the two (or both) EOS models. Depending on the poorly known ionization degree, the Kramers-Unsöld formula may still be not applicable at this time, and then the agreement would be simply fortuitous, due to the nearly constant T_e value in the outer layer of the rarefaction wave. If the time is too short for the Kramers-Unsöld formula to be applicable, one would expect that the emission signal calculated with it must be higher than (or close to) the observed signal because the layer $\tau_{\mathrm{KU}}\simeq 1$ lies deeper than the actual emitting layer and should, therefore, have a higher electron temperature. Hence only when the Kramers-Unsöld intensity turns out to be significantly lower than the observed signal should it be interpreted as an indication that the EOS model is not adequate for the unloading plasma. We do not find such an inconsistency between our experimental results and either SESAME or our EOS model.

Turning the above argument around, one might speculate also that the agreement between the observed and calculated Kramers-Unsöld signals indicates that the ionization degree of aluminum at $T_e\simeq 1$ eV and $\rho\simeq 1$ g/cm^3 is in fact significantly below 1, i.e., much less than in the present simulations.

[1] Ya. B. Zel'dovich and Yu. P. Raizer, *Physics of Shock Waves and High Temperature Hydrodynamic Phenomena* (Academic, New York, 1966).

[2] L. V. Al'tshuler, Sov. Phys. Usp. **8**, 52 (1965).

[3] *LASL Shock Hugoniot Data*, edited by S. P. Marsh (University of California Press, Berkeley, 1980).

[4] P. Celliers and A. Ng, Phys. Rev. E **47**, 3547 (1993).

[5] E. M. Campbell, Laser Part. Beams **9**, 209 (1991); R. Cauble, D. W. Phillion, T. J. Hoover, N. C. Holmes, J. D. Kilkenny, and R. W. Lee, Phys. Rev. Lett. **70**, 2102 (1993); R. L. Kaufmann, L. J. Suter, C. B. Darrow, J. D. Kilkenny, H. N. Kornblum, D. S. Montgomery, D. W. Phillion, M. D. Rosen, A. R. Theissen, R. J. Wallace, and F. Ze, *ibid.* **72**, 2320 (1994).

[6] Th. Löwer, R. Sigel, K. Eidmann, I. B. Földes, S. Hüller, J. Massen, G. D. Tsakiris, S. Witkowski, W. Preuss, H. Nishimura, H. Shigara, Y. Kato, S. Nakai, and T. Endo, Phys. Rev. Lett. **72**, 3186 (1994).

[7] P. Celliers, A. Ng, G. Xu, and A. Forsman, Phys. Rev. Lett. **68**, 2305 (1992).

[8] A. Ng, P. Celliers, G. Xu, and A. Forsman, Phys. Rev. E **52**, 4299 (1995).

[9] C. Kittel, *Introduction to Solid State Physics*, 5th ed. (Wiley, New York, 1976).

[10] SESAME Report on the Los Alamos Equation-of-State Library, Report No. LALP-83-4, T4 Group LANL, Los Alamos, 1983 (unpublished).

[11] Yu. P. Raizer, Sov. Phys. JETP **9**, 1124 (1959).

[12] R. M. More, in *Physics of Laser Plasma*, edited by A. Rubenchik and S. Witkowski, Handbook of Plasma Physics, Vol. 3 (North-Holland, Amsterdam, 1991), p. 63.

[13] S. B. Kormer, A. I. Funtikov, V. D. Urlin, and A. N. Kolesnikova, Sov. Phys. JETP **42**, 686 (1962).

[14] E. M. Lifshitz and L. P. Pitaevskii, *Physical Kinetics* (Pergamon, Oxford, 1981).

[15] H. Brysk, P. M. Campbell, and P. Hammerling, Plasma Phys. **17**, 473 (1975).

[16] W. B. Hubbard, Astrophys. J. **146**, 858 (1966).

[17] D. G. Yakovlev and V. A. Urpin, Sov. Astron. **24(3)**, 303 (1980).

[18] Y. T. Lee and R. M. More, Phys. Fluids **27**, 1273 (1984).

[19] L. Spitzer, *Physics of Fully Ionized Gases* (Interscience, New York, 1956).

[20] M. Lampe, Phys. Rev. **170**, 306 (1968).

[21] *CRC Handbook of Chemistry and Physics*, edited by D. R. Lide (CRC, Boca Raton, 1994).

[22] H. Brysk, Plasma Phys. **16**, 927 (1974).

[23] H. E. Elsayed-Ali, T. B. Norris, M. A. Pessot, and G. A. Mourou, Phys. Rev. Lett. **58**, 1212 (1987).

[24] P. B. Corkum, F. Brunel, N. K. Sherman, and T. Srinivasan-Rao, Phys. Rev. Lett. **61**, 2886 (1988).

[25] R. H. M. Groeneveld, R. Spirk, and A. Lagendijk, Phys. Rev. Lett. **64**, 784 (1990).

[26] M. Basko, Nucl. Fusion **30**, 2443 (1990).

[27] M. Born and E. Wolf, *Principles of Optics*, 6th ed. (Pergamon, Oxford, 1980).

[28] Th. Löwer, R. Sigel, M. Basko, and R. Ramis (unpublished).

[29] A. Ng, D. Parfeniuk, P. Celliers, L. DaSilva, R. M. More, and Y. T. Lee, Phys. Rev. Lett. **57**, 1595 (1986).

[30] J. J. Duderstadt and G. A. Moses, *Inertial Confinement Fusion* (Wiley, New York, 1982).